INTERNATIONAL JOURNAL FOR NUMERICAL METHODS IN FLUIDS
Int. J. Numer. Meth. Fluids 2003; **42**:163–186 (DOI: 10.1002/fld.478)

Computational study of unsteady turbulent flows around oscillating and ramping aerofoils

G. N. Barakos*,† and D. Drikakis‡

Engineering Department, Queen Mary, University of London, London E1 4NS, U.K.

SUMMARY

The aim of this work is to computationally investigate subsonic and transonic turbulent flows around oscillating and ramping aerofoils under dynamic-stall conditions. The investigation is based on a high-resolution Godunov-type method and several turbulence closures. The Navier–Stokes and turbulence transport equations are solved in a strongly coupled fashion via an implicit-unfactored scheme. We present results from several computations of flows around oscillating and ramping aerofoils at various conditions in order to (i) assess the accuracy of different turbulence models and (ii) contribute towards a better understanding of dynamic-stall flows. The results show that the employed non-linear eddy-viscosity model generally improves the accuracy of the computations compared to linear models, but at low incidence angles the Spalart–Allmaras one-equation model was found to provide adequate results. Further, the computations reveal strong similarities between laminar and high-Reynolds number dynamic-stall flows as well as between ramping and oscillating aerofoil cases. Investigation of the Mach number effects on dynamic-stall reveals a delay of the stall angle within a range of Mach numbers. Investigation of the reduced frequency effects suggests the existence of an (almost) linear variation between pitch rate and stall angle, with higher slope at lower pitch rates. The pitch rate affects both the onset of dynamic-stall as well as the evolution of the associated vortical structures. Copyright © 2003 John Wiley & Sons, Ltd.

1. INTRODUCTION

In the context of aerodynamics, the numerical simulation of unsteady, turbulent and compressible flows around moving boundaries is motivated by the need to understand flow phenomena associated with the behaviour of aircrafts during manoeuvres, as well as flows around helicopter rotors and turbomachinery blades. The flow phenomena appearing in the above

* Correspondence to: G.N. Barakos, CFD Laboratory, Department of Aerospace Engineering, University of Glasgow, Glasgow G12 8QQ, U.K.
† E-mail: gbarakos@aero.gla.ac.uk
‡ E-mail: d.drikakis@qmw.ac.uk

Contract/grant sponsor: EP-SRC/MoD; contract/grant number: GR/L18457
Contract/grant sponsor: Brite/EuRam project UNSI
Contract/grant sponsor: European Union; contract/grant number: BRPR-CT97-0583

Received April 2001
Revised 18 November 2002

applications are highly non-linear due to the presence of separation, unsteadiness, shock/boundary layer, viscous/inviscid, vortex/body and vortex/vortex interactions, transition to turbulence and flow re-laminarization. A better understanding of the flow physics in the aforementioned applications will possibly enable us to control the flow and, subsequently, enhance the performance of airplanes and helicopters.

The cost of performing wind tunnel or flight experiments in unsteady flows is very high. Moreover, the information obtained through experiments is usually limited—due to the instrumentation constraints—to pressure distributions or aerodynamic coefficients, though developments in experimental techniques (PIV, LDA, etc.) may push further forward the current state of the art of experiments in unsteady flows. Numerical simulation of unsteady flows is a promising alternative, but it is not free of shortcomings and difficulties; these are primarily related to numerical and turbulence modelling limitations. At the most advanced computational level, turbulent flows can be studied by performing direct numerical simulation (DNS). DNS requires large computing resources and it is so far applicable only at low Reynolds numbers. An alternative could be the large eddy simulation (LES). However, three-dimensional computations still need to be performed and this would require large computing resources, though less than DNS; moreover, careful modelling, especially of the near-wall flow, still remains an open issue in both LES and RANS computations. For the time being, unsteady Reynolds-averaged Navier–Stokes simulations (URANS) seem to be the only feasible way for simulating flows around moving aerofoils at Reynolds numbers of the order of 10^6–10^7.

One of the major challenges in the computation of unsteady aerodynamic flows is the accurate prediction of the *dynamic-stall* (DS) phenomenon. This appears in high-angle manoeuvres and is caused by the development of an energetic vortical structure known as *dynamic-stall vortex* (DSV). Accurate prediction and, possibly, control of dynamic stall can enhance the performance in various engineering applications. For example, the manoeuvrability of fighter aircrafts could be enhanced if the unsteady airloads generated by DS are utilized in a controlled manner. Effective stall control of the retreating blade of a helicopter rotor could also increase the maximum flight speed by reducing rotor vibrations and power requirements. Similarly, by controlling DS the maximum speed of wind mills or turbine rotors can be increased resulting, subsequently, in more efficient production of electrical energy and reduction of vibration. The phenomenon of dynamic stall can be studied by considering the pitching motion of an aerofoil beyond its static-stall incidence angle. As a result of the pitching motion, the dynamic-stall vortex is formed and is subsequently accompanied by additional vortices emerging from the leading and trailing edge of the aerofoil. During the pitching motion, large variations of the aerofoil's aerodynamic loads occur.

Reviews of past experimental works can be found in the papers of Telionis [1] and McCroskey *et al.* [2–5], while another experimental study was more recently published by Piziali [6]. Doligalski *et al.* [7] have also reviewed theoretical work on vortex interaction and separation including dynamic stall. Analytical studies include the investigation of linear and non-linear instability of a leading edge separation by Smith [8] and the interaction of a vortex with a boundary layer by Peridier *et al.* [9].

Past studies include the investigation of dynamic stall in laminar flows, e.g. References [10–12] and references therein, as well as in turbulent flows, e.g. References [13–21]. The studies concerned with turbulent flows have been performed using algebraic, one-equation, as well as high-Re k–ε and k–ω models while there is a limited number of studies employing more advanced turbulence closures [21].

Past research on steady turbulent flows has shown that the accuracy of numerical predictions is significantly affected by the accuracy of the turbulence model employed. Experience using zero-equation turbulence models (e.g. Reference [22]) has shown that these models do not provide satisfactory results, especially in separated flows. Linear eddy-viscosity models provide satisfactory results for attached, fully developed turbulent boundary layers with weak pressure gradients and are also relatively easy to implement into computational fluid dynamics (CFD) codes. Linear low-Re two-equation models seem to offer the best balance between accuracy and computational cost, but since they employ the Boussinesq approximation for the Reynolds stress tensor, they are not able to capture effects arising from normal-stress anisotropy. Second-moment closures offer a more exact representation of the Reynolds stresses but require longer computing times and careful numerical implementation for obtaining stable numerical solutions. Reynolds-stress models have been used in the past to investigate shock/boundary-layer interaction (see References [23, 24], amongst others). These studies have shown that in certain cases second-moment closures may provide better results than linear models, but in other cases the results are inconclusive. Other approaches in turbulence modelling include the non-linear eddy viscosity models (NLEVM) [25, 26] and explicit algebraic stress models (see References [27–29]).

NLEVMs is one of the approaches employed in this study. The objective of this approach is to introduce closures that incorporate key features of the Reynolds-stress models, but which; however, require computational effort comparable to linear two-equation eddy-viscosity models [25, 30–32]. Other attempts to use advanced turbulence models in aerodynamic flows can be found in the works of Gatski [27], Jiang *et al.* [33], and Barakos and Drikakis [21, 34, 35]. The experience from steady flows has shown that NLEVMs offer some promising capabilities in terms of accuracy and, additionally, are more economic in terms of computing resources compared to the Reynolds-stress transport models. Non-linear models have been and are still being refined and validated for steady flows, mainly two-dimensional and incompressible (see References [26, 36]) while some experience has also been acquired from applications to compressible flows, e.g. References [24, 27, 34, 35].

In addition to turbulence modelling, other challenges are associated with the robustness of numerical methods employed for the time integration of the Navier–Stokes and turbulence transport equations. Computations of flows around moving boundaries are demanding in terms of computing time and, therefore, numerical issues in connection with the time integration of the Navier–Stokes equations require careful consideration. In the past, many researchers have developed Navier–Stokes methods for unsteady inviscid and viscous flows based on explicit, implicit approximate-factorization or hybrid schemes, e.g. References [15, 16]. Explicit schemes require the use of very small time steps which lead to long computing times. Approximate-factorization schemes allow larger time steps, but still pose stringent constraints regarding the maximum Courant–Friedrichs–Lewy (CFL) number, especially in three-dimensional flows. On the other hand, implicit-unfactored schemes which use Newton sub-iterations allow larger CFL numbers and are less sensitive to the choice of time step than approximate-factorization schemes [37]. Concerning the discretization scheme, the state-of-the-art numerical methods used in the simulation of compressible flows have principally been developed for the Euler equations of gas dynamics and have been designed to account only for the mean flow variables. The authors have developed a Godunov-type method which accounts directly for the turbulence flow quantities, and have investigated the method's performance in conjunction with eddy-viscosity models [38]. The coupling of turbulence and

mean flow equations was found to be of particular importance in the case of unsteady flows since it avoids the use of two different time steps which, depending on the case, may lead to numerical instabilities. The Godunov-type method and implicit-unfactored scheme of [20, 38] form the computational basis of the present study.

The objectives of the present work are (i) to assess the accuracy of different turbulence models in dynamic-stall flows around oscillating and ramping aerofoils, (ii) to study dynamic-stall flows for a range of flow conditions, and (iii) to investigate the Mach number and reduced frequency effects for the flows in question. The paper is organized as follows. Section 2 presents the governing equations, numerical method and turbulence models used in this study. In Section 3 we present results from several flow computations including small amplitude oscillating flows at subsonic and transonic Mach numbers, as well as dynamic-stall flows at high amplitude, high mean incidence angle. Further, we discuss the effects of the reduced frequency and Mach number on the above flows. The purpose of the computations is to present the extended range of conditions over which dynamic stall occurs, as well as to highlight the dependence of the predictions on the employed turbulence models. Wherever possible, direct comparisons with experimental results are presented. In Section 4 we discuss the flow development under dynamic-stall conditions around ramping and oscillating aerofoils by looking into the whole spectrum of computations performed in the course of the present work. Finally, Section 5 summarizes the conclusions drawn from our investigation.

2. MATHEMATICAL MODELLING

In this section, we briefly present the governing equations, turbulence models and numerical method used. Details about the numerical scheme can be found in References [20, 38].

2.1. Governing equations

The governing equations employed here are the two-dimensional, unsteady Reynolds-averaged, compressible Navier–Stokes equations. Additional equations are required to model turbulence transport. The governing equations are solved in a non-inertial frame of reference (NIFR) (Figure 1).

For all test cases presented in this work the aerofoil performs either a harmonic oscillation or a ramping motion about its quarter-chord axis (Figure 1). The harmonic oscillation is given in terms of the angle-of-incidence, $\alpha(t)$, by

$$\alpha(t) = \alpha_0 + \alpha_1 \sin(\omega_f t) \tag{1}$$

where α_0 and α_1 are the mean angle and amplitude of the harmonic oscillation, respectively. In the case of oscillating aerofoils, the unsteady motion is usually characterized by the similarity parameter k_f, known as reduced frequency of the oscillation; this is defined by

$$k_f = \omega_f c / 2U_\infty \tag{2}$$

where c is the aerofoil chord, ω_f is the frequency of the oscillation and U_∞ is the free-stream velocity. For the ramping cases the variation of the incidence angle is given by

$$\alpha(t) = \alpha_0 + \dot{\alpha} t \tag{3}$$

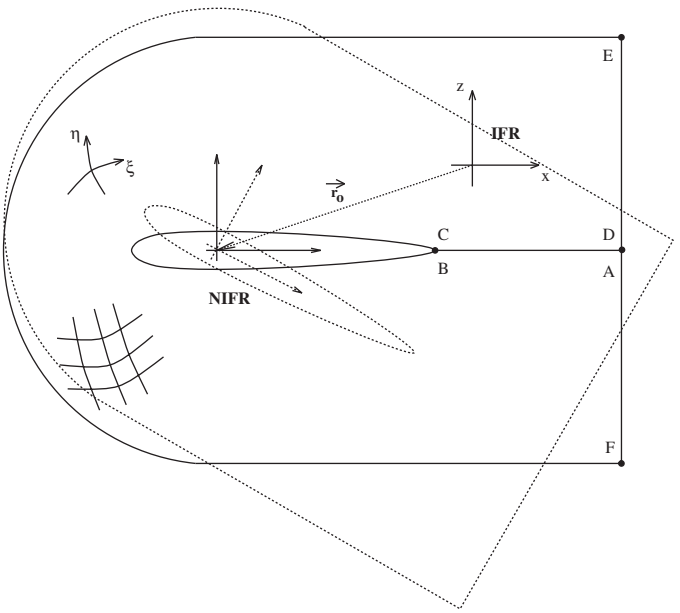

Figure 1. Schematic of the flow domain.

The pitch rate is non-dimensionalized as

$$k_f = \dot{\alpha} c / U_\infty \tag{4}$$

where $\dot{\alpha}$ is the pitch rate in degrees per second. Both the harmonic oscillating and ramping cases are hereafter referred to as *pitching aerofoil cases*.

For the simulation of unsteady flows around pitching aerofoils, we employ the URANS equations for a compressible fluid:

$$\frac{\partial \rho}{\partial t} + \frac{\partial}{\partial x_i}(\rho u_i) = 0 \tag{5}$$

$$\frac{\partial \rho u_i}{\partial t} + \frac{\partial}{\partial x_i}(\rho u_i U_j + p\delta_{ij} - \tau_{ij}) = 0 \tag{6}$$

$$\frac{\partial \rho e}{\partial t} + \frac{\partial}{\partial x_i}(\rho U_i (e + p) - u_i \tau_{ij} - \dot{q}_i) = 0 \tag{7}$$

$$U_i = u_i - u_i^g \tag{8}$$

where u_i $(i = 1, 2)$ are the fluid velocity components, u_i^g $(i = 1, 2)$ are the velocity components due to the motion of the computational grid, p is the pressure, ρ is the density and e is the total energy per unit volume. The pressure is calculated by the ideal gas equation of state ($p = \rho RT$; R is the gas constant and T is the temperature) and τ_{ij} is obtained by the sum of the laminar and Reynolds stress tensors. To close the above system of equations, the

definitions of the turbulent Reynolds stresses and heat fluxes ($\dot{q}_i$) as functions of the mean flow quantities are required. For the linear EVM, the stress tensor is defined according to the Boussinesq approximation, i.e. it is proportional to the mean strain-rate tensor, with the factor of proportionality being the eddy viscosity (μ_T). The eddy viscosity is modelled in terms of the turbulent kinetic energy and a turbulence scale variable, the latter being dependent on the model employed (see Section 2.2). The total stresses and heat fluxes for the case of linear EVMs are calculated as follows:

$$\tau_{ij} = \tau_{lij} + \tau_{tij} \tag{9}$$

$$\tau_{lij} = \mu(S_{ij} - S_{nn}\delta_{ij}/3) \tag{10}$$

$$\tau_{tij} = \mu_T(S_{ij} - S_{nn}\delta_{ij}/3) - 2\rho k\delta_{ij}/3 \tag{11}$$

where $S_{ij} = (U_{i,j} + U_{j,i})/2$ is the mean strain rate, k is the kinetic energy of turbulence, and μ is the dynamic viscosity of the fluid. The heat flux rates are modelled according to the Fourier's law:

$$\dot{q}_i = \dot{q}_{li} + \dot{q}_{ti} = -\left(\frac{\mu}{Pr} + \frac{\mu_T}{Pr_T}\right)\frac{\partial T}{\partial x_i} \tag{12}$$

where Pr and Pr_T are the laminar and turbulent Prandtl numbers, respectively. The turbulence models employed here are discussed in the next section.

2.2. Turbulence modelling

The stress tensor $\tau_{ij} = \tau_{lij} + \tau_{tij}$ contains molecular and Reynolds-stress contributions. Linear eddy-viscosity models of the k–ε type require the solution of two transport equations, one for the kinetic energy of turbulence, k, and one for the turbulent dissipation rate, ε, or its isotropic component $\tilde{\varepsilon}$ ($\tilde{\varepsilon} \equiv \varepsilon - \hat{\varepsilon}$, $\hat{\varepsilon} \equiv 2\mu/\rho(\partial\sqrt{k}/\partial x_j)^2$). These models make use of the Boussinesq approximation to model the Reynolds-stress tensor. According to Fan *et al.* [39], for turbulent flows far from equilibrium, like the unsteady flows investigated in the present paper, it is suggested to avoid the use of the parameter y^+ ($y^+ = y\rho u_\tau/\mu$, where y is the distance from the solid boundary and u_τ is the friction velocity) in the near-wall formulation of the turbulence models. Instead, the turbulent Reynolds number or, alternatively, the near-wall Reynolds number should be used. In view of the above, the following LEVMs have been employed in this study: (i) the one-equation turbulence model of Spalart and Allmaras (SA) [40], (ii) the linear low-Re k–ε EVMs of Launder and Sharma (LS) [41] and Fan *et al.* [39].

Further, we have employed NLEVMs which use an expansion of the Reynolds-stress components with respect to the mean strain-rate S_{ij} and rotation $\Omega_{ij} = (U_{i,j} - U_{j,i})/2$ tensors. Craft *et al.* [36] and Suga [42] developed a low-Re, cubic non-linear eddy viscosity model and applied it to incompressible flows. Their studies indicate that the model is able to give results close to the ones obtained by second-moment closures. The detailed formulation of the employed NLEVM can be found in the paper of Craft *et al.* [26] and, thus, are not repeated here. The performance of the NLEVMs in steady shock/boundary-layer interaction has been discussed in Reference [34]. Although in this study we do not aim to carry out a detailed investigation of second-moment closures, some comparisons between the Launder–

Shima Reynolds-stress transport model (RSTM) [43] and the EVM models, are also presented in the results section.

2.3. Numerical method

A detailed description of the numerical method employed here can be found in the papers of Barakos and Drikakis [20, 38]. A brief description of the method is given below.

We solve the conservation equations of mass, momentum and energy in conjunction with the turbulence-transport equations using a finite volume approach and body-fitted curvilinear co-ordinates. A Godunov-type method [38, 44–46] is used for discretizing the advective fluxes. Limiters based on the squares of pressure derivatives are employed for detecting shocks and contact discontinuities. The viscous terms are discretized by central differences.

Careful consideration has been given to the time integration of the equations. Both explicit and implicit schemes have been implemented into the present CFD code [38] and their efficiency is strongly dependent on the time scales imposed by the prescribed motion of the solid boundaries. In this study, we solve the six or nine equations (in the case of second-moment closure) in a strongly coupled fashion by an implicit-unfactored method which combines Newton sub-iterations and point Gauss–Seidel relaxation. The implicit-unfactored implementation enables us to achieve convergence in the case of complex turbulence models which contain stiff source terms, e.g. NLEVMs. The method requires a moderate number of Newton iterations (40–500, depending on the flow case) at each time step. In unsteady flows the steady-state solution around a fixed boundary is given as initial condition [20]. Additionally, to achieve large CFL numbers, preconditioning of the inversion matrix is performed at each Gauss–Seidel sub-iteration [38].

3. COMPUTATION OF DYNAMIC STALL FLOWS

Several flow cases around pitching aerofoils, ranging from subsonic to transonic and from laminar to turbulent flow conditions, have been computed in order to assess the accuracy of turbulence models and provide quantitative and qualitative information about the flow development under dynamic stall conditions.

Three different aerofoils were employed in the computations namely, the NACA-0012, NACA-0015 and NACA-64A010, for which experimental data are available, e.g. Reference [6].

The computations have been performed using body-fitted, structured C-type grids. The grid have been generated using an elliptic grid generation method [47]; it contains 200 cells on the aerofoil's surface, 50 cells along each side of the artificial boundary behind the aerofoil's trailing edge (lines AB and CD in Figure 1) and 90 cells in the vertical direction. A coarser mesh with 180×80 grid points has been used for the one-equation SA model. The grid lines have been clustered close to the aerofoil's surface in the direction normal to the wall as well as around the leading and trailing edges of the aerofoil. In all computations, the first grid node above the solid boundary was placed at a distance of $10^{-6}c$, resulting in $y^+ < 1$. The far-field boundary was placed at $6c$ in the upstream direction and at $10c$ in the wake direction. Characteristic boundary conditions are posed around the computational domain. The above dimensions of the computational domain in combination with characteristic boundary

Table I. Summary of the validation cases.

Case	Aerofoil	M_∞	Re_c	k_f	α_0	α_1	$(x/c)_{rot}$	$(x/c)_{trip}$
			Oscillating					
1 (CT1)	0012	0.6	4.8×10^6	0.16	2.8	2.4	0.25	0.1
2	64A010	0.796	12.56×10^6	0.202	0	1.01	0.248	0.1
3	0015	0.29	1.95×10^6	0.1	17	4.2	0.25	0.2
			Ramping					
5	0012	0.56	4.5×10^6	0.85	−4.0	30	0.25	0.1

conditions have been found to be sufficient for avoiding numerical effects on the flow solution, e.g. reflection of pressure waves at the boundaries.

The level of the free-stream turbulence has been kept constant at 0.5% of the kinetic energy of the incoming stream. A length scale of $0.01c$ has been used to estimate the free stream value of the turbulence energy dissipation rate. As initial conditions, the steady-state solution of the flow around the aerofoil has been used. A summary of the test cases is given in Table I. The validation of the models for each case is discussed below.

3.1. Small amplitude oscillations versus dynamic stall

The first case is the unsteady transonic flow around a NACA-0012 aerofoil with Mach and Reynolds numbers of 0.6 and 4.8×10^6, respectively. The mean incidence angle is 2.8° and the amplitude of oscillation is 2.4°. The aerofoil performs pitching motion with respect to the quarter-chord axis ($x/c = 0.25$) at a reduced frequency of 0.16. The case is identified as CT1 in the AGARD compendium of unsteady aerodynamic measurements [48]. The results for the lift and moment loops are shown in Figures 2(a) and 2(b) for the linear EVM model of Fan *et al.* [41] (FLB), the NLEVM of Craft *et al.* [26] and the RSTM of Launder and Shima [43]. Because of the high value of the freestream Mach number, a shock appears in the leading edge region of the aerofoil. The strength of the shock changes as the aerofoil oscillates. The differences between different models predictions are reflected on the moment loop where discrepancies between numerical predictions and experimental data are shown. Detailed comparisons between experiments and simulations for the instantaneous C_p distributions are presented in Figures 2(c)–2(f). Differences between the model predictions are encountered only in the shock region; the differences are subsequently reflected on the C_l and C_m coefficients. Comparing the CPU time required for each of the above models, the second moment closure was found to be the most demanding. For the present flow case, the RSTM, NLEVM and LEVM models require 16.2, 9.5 and 8.9 work units (one work unit corresponds to a minute of CPU time on a HP 9000/700/99 workstation), respectively. On the other hand, for all cases considered in the present paper the results for the aerodymanic loads obtained by the RSTM were almost identical with those predicted by the NLEVM.[§] In view of the

[§]We should point out that a thorough assessment of second-moment closures requires experimental data for the turbulent stresses; such data are not however available yet for the flows in question.

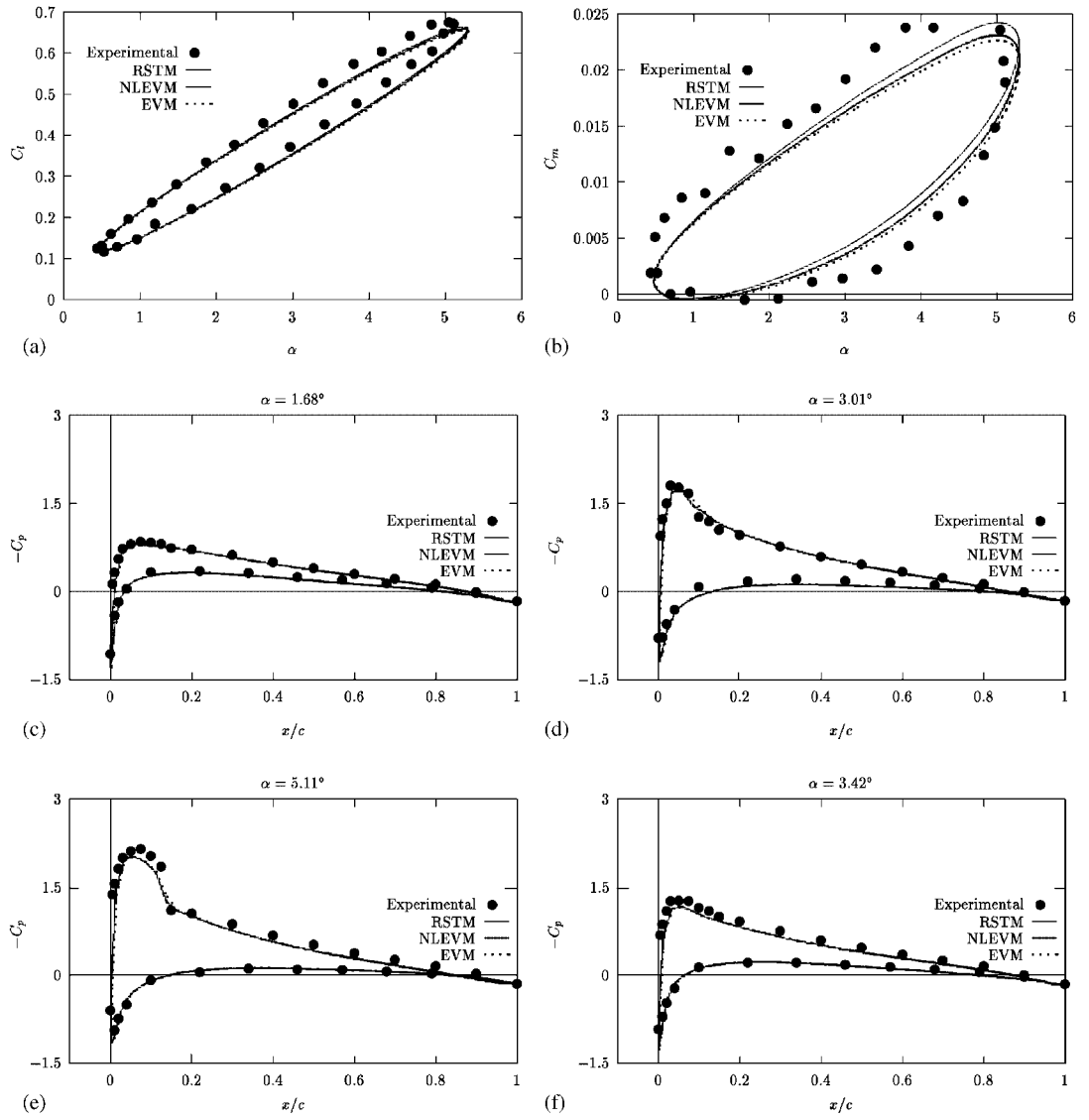

Figure 2. Comparisons of various models for the AGARD CT-1 case. (a) C_l loop, (b) C_m loop, (c)–(f) instantaneous C_p curves.

above, for the rest of the validation cases we present only the results obtained by the linear and non-linear eddy-viscosity models.

The second validation case is the transonic flow around an oscillating NACA-64A010 aerofoil. The flow conditions correspond to Reynolds and Mach numbers 12.56×10^6 and 0.796, respectively, and experimental data are available [48] for the hysteresis loops and instantaneous surface pressure distributions at various incidence angles. The mean incidence and

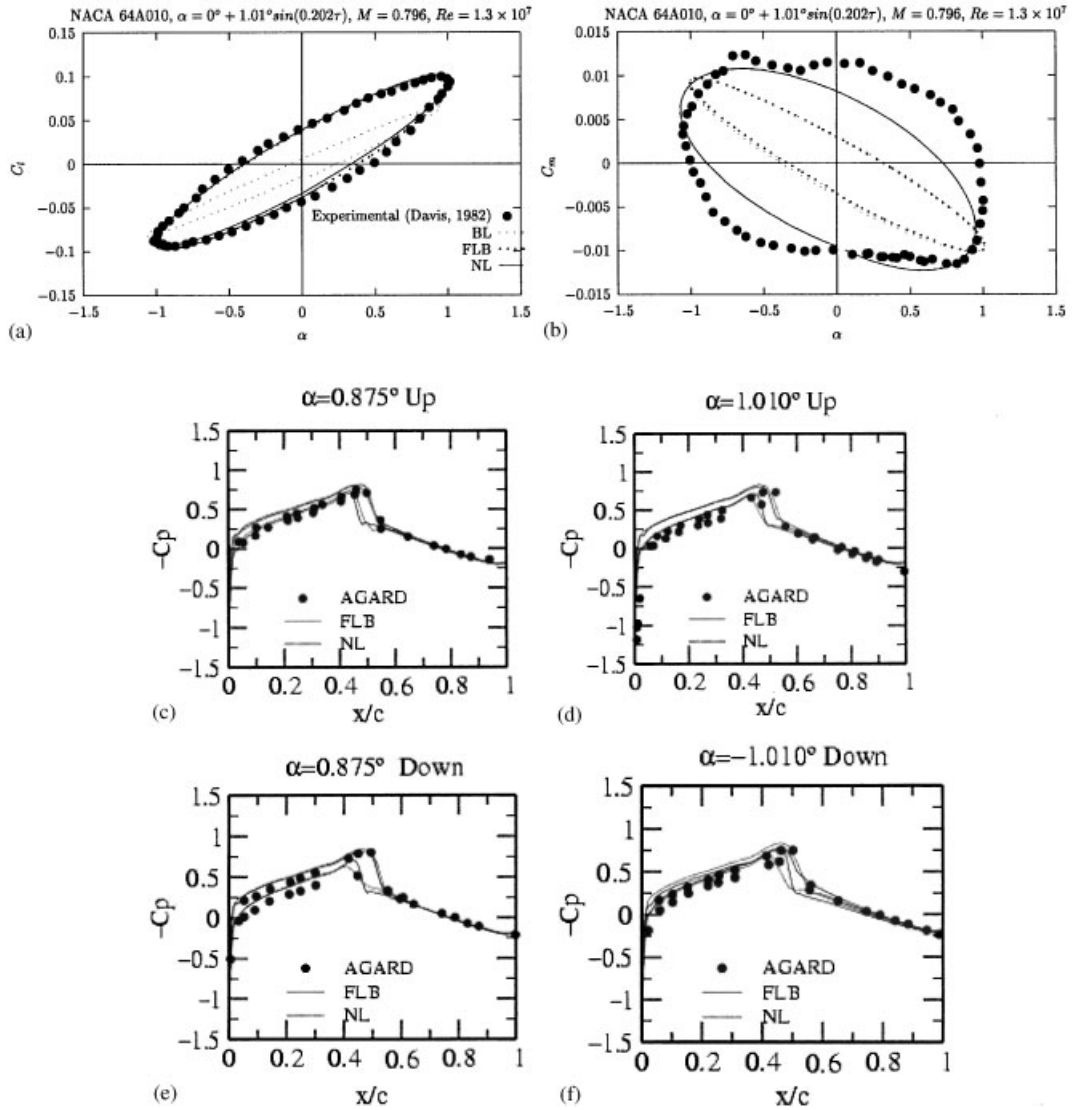

Figure 3. Comparisons of different models for the oscillating NACA-64A010 at transonic flow conditions. (a) C_l loop, (b) C_m loop, (c)–(f) instantaneous C_p curves.

oscillation amplitudes are 0 and 1.01°, respectively. The reduced frequency of the oscillation is $k_f = 0.202$. For this flow case, shock waves appear both on the pressure and suction sides of the aerofoil, and their relative strength and position changes as the aerofoil oscillates.

Comparisons between the algebraic Baldwin–Lomax [22], the Fan *et al.* [39] (FLB) k–ε model, and the NLEVM of Craft *et al.* [26] (NL) are shown in Figure 3 for the lift and moment loops. The NLEVM provides better results, especially for the C_m loop. This

is also associated with the better results provided by the NLEVM for the shock positions on the pressure and suction sides of the aerofoil; this can be seen in the instantaneous C_p distributions (Figures 3(c)–(f)).

The third case is a deep-stall computation around the NACA-0015 aerofoil. Experiments for this aerofoil have been performed by Piziali [6], and these were used herein. The experimental results include hysteresis loops of the lift, drag, and moment coefficients. The data correspond to deep-stall conditions at which the static-stall angle is exceeded.

In order to carry out the unsteady computations, the quasi-steady turbulent flow around the aerofoil at mean incidence angle is computed first, and the solution is given as initial condition to the unsteady-flow calculation. The free-stream conditions correspond to a Reynolds number of 1.95×10^6 and a Mach number of 0.29. The amplitude of the oscillation is 4.2°, the mean incidence is 17° and the reduced frequency of the oscillation is $k_f = 0.1$. The Spalart–Allmaras (SA) [40], the Launder–Sharma (LS) [41] linear k–ε and the Craft *et al.* NLEVM model (NL) [26] are employed in the computations. Quasi-steady computations (not shown here) indicated that all models predict stalled flow for incidence angles about 13°. Therefore, only unsteady solutions should be carried-out for higher incidence angles.

Results for the unsteady airload hysteresis loops are shown in Figure 4. The comparisons with the experimental results show that the NLEVM improves the predictions compared to LEVMs, but the differences with the experiment still remain large. The linear model leads to excessive production of turbulence, whereas the NLEVM predicts lower levels of turbulence, and thus the dynamic-stall vortex (DSV) separates more readily. The results show that the predictions of the NLEVM and SA models are comparable for some parts of the unsteady cycle, except for the higher values of the incident angle where the NLEVM results are closer to the experimental data. The differences between the models are more pronounced in the moment loop. The results for the moment coefficient are better predicted by the NL model, but discrepancies between computations and experiment still exist.

We note that in contrast to the previous AGARD cases, in the dynamic stall case of the NACA-0015 the aerofoil exhibits higher lift during the upstroke motion than during the downstroke. The situation is reversed in small amplitude oscillations where the flow is essentially attached and the aerodynamic loops are mainly associated with the hysteresis of the boundary layer's response to the motion of the lifting surface.

3.2. Mach number and pitch-rate effects

We have performed an investigation of the Mach number and pitch-rate effects for a ramping NACA-0012 aerofoils. In the past, several experimental investigations have been carried out in connection with ramping NACA 0012 aerofoils [48–50]. Here, we have performed computations for $M_\infty = 0.56$ and $Re = 4.5 \times 10^6$ and for a dimensionless pitch rate of 0.85°/s; this pitch rate allows all calculations to be in the dynamic-stall regime. The incidence angle varies from 0° to a maximum of 30°. This case was selected because it combines relatively high Mach number and stall, the latter occuring at high incidence angles. Figure 5 compares the Mach-scaled lift coefficient as predicted by linear and non-linear EVMs, with experimental results from [48]. Comparisons between simulation results and experimental data for the pressure coefficient distributions at three different time instants are also shown in the same figure. At low angles of incidence, the flow is attached, and both models predict almost perfectly the experimental values. At higher incidence angles, where a shock is formed close to the

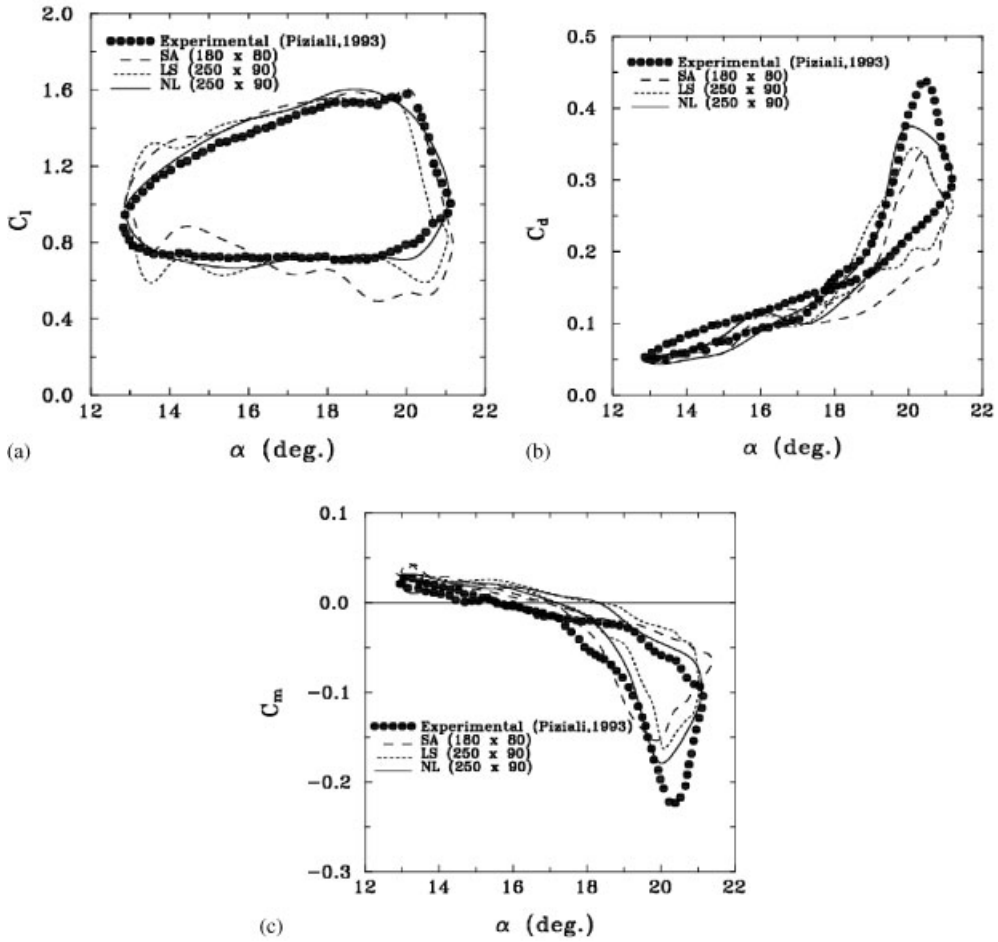

Figure 4. Comparison of linear (LS) and non-linear (NL) eddy-viscosity models for the unsteady airloads of the NACA-0015 aerofoil.

leading edge of the aerofoil, the NLEVM provides better predictions, though there are still significant discrepancies between the numerical results and the experiment. After the stall, and as the aerofoil reaches the maximum incidence, the predictions of the models start to converge again, but discrepancies with the experimental data still exist, especially close to the leading edge of the aerofoil (Figure 5(d)).

Using the above flow case, we performed an investigation of the Mach number effects on the stall angle. Past experimental studies [51] have shown that at high Mach numbers ($M_\infty > 0.45$) the shock suppresses the onset of the separation bubble at the leading edge of the profile and the stall mechanism is initiated by shock/boundary-layer interaction, in contrast to lower Mach numbers ($M_\infty < 0.45$) where the dynamic stall initiates from adverse-pressure-gradient separation. Here, we performed calculations at Mach numbers of 0.46, 0.56, 0.66 and 0.76 and the lift curves are shown in Figure 5(e). The increase of Mach number results in a

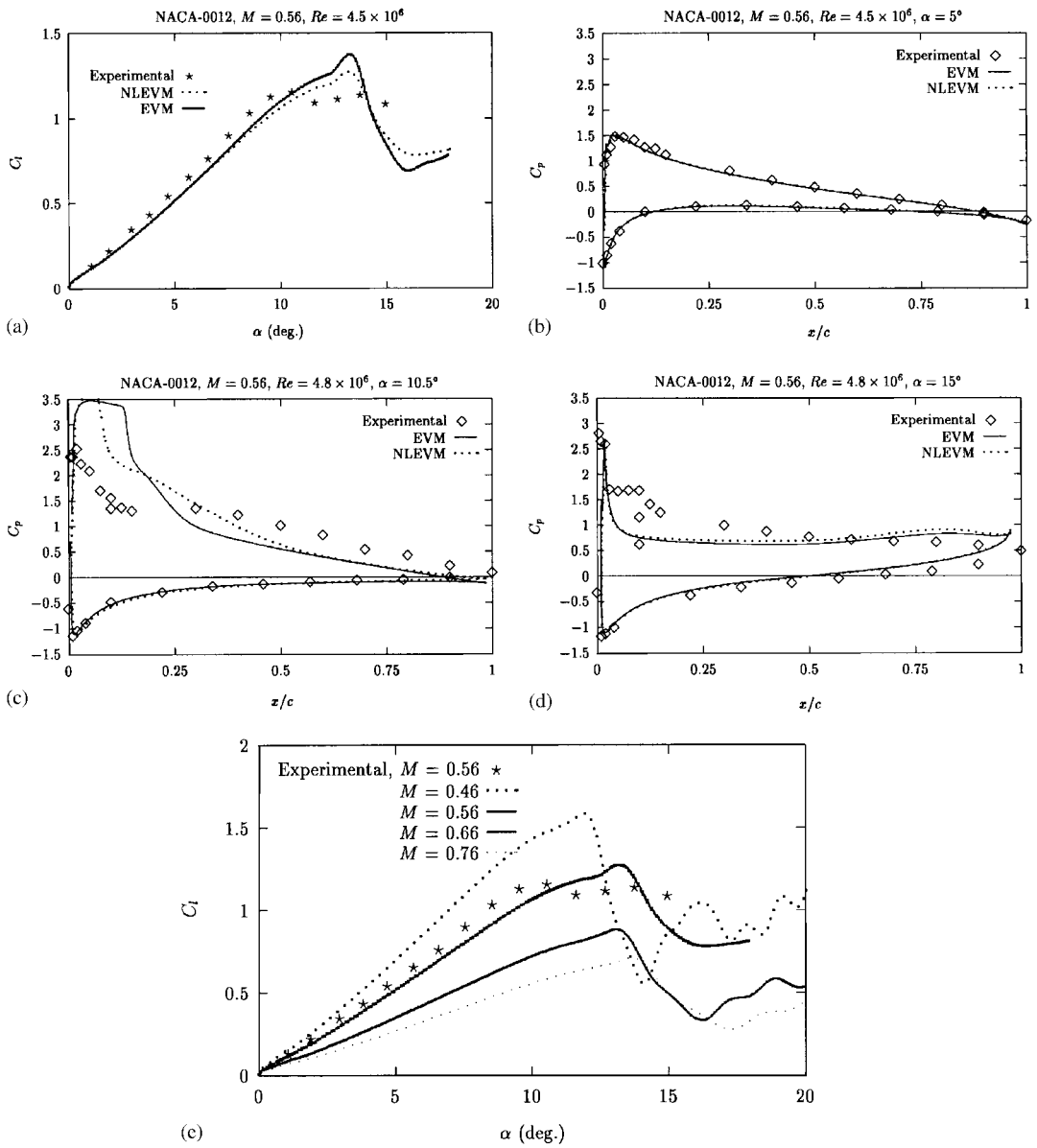

Figure 5. Ramping NACA-0012: (a) lift curve, and comparison between the numerical and experimental results for the C_p coefficient at (b) 5°, (c) 10.5°, (d) 15°; (e) Mach number effects on the lift for a ramping NACA-0012 aerofoil.

reduction of the maximum lift as well as in a slight change of the stall angle. The values of the maximum lift coefficient and stall angles are also given in Table II. The present results are in agreement with previous calculations by Choudhuri and Knight [12] who also reported a delay of the stall angle when increasing the Mach number.

Table II. Maximum lift coefficient and stall angle for a ramping NACA-0012 aerofoil at various Mach numbers ($Re = 4.5 \times 10^6$, $\alpha_0 = -4^\circ$, $\alpha_1 = 30^\circ$, $k_f = 0.85$).

Mach Number	Max. C_l	α_{stall}
0.46	1.58	11.8
0.56	1.27	12.4
0.66	0.56	13.7
0.76	0.71	14.3

One of the most important parameters in unsteady flows around ramping and oscillating aerofoils is the speed of the induced motion of the profile, since this constitutes the driving mechanism of the DS phenomenon. Wilby [49] analysed data from several experiments for rapidly ramping aerofoils and showed that the dependence of the stall angle on the ramping rate can be represented by a curve with two branches (Figure 6(a)). For high pitch rates, there is an almost linear relationship between pitch rate and stall angle. The same also applies to low pitch rates, but the linear relationship has a different slope. According to Wilby [49], there is a region of pitch rates where the two curves intersect, marking clearly that, at low pitch rates, there is a definite change of the phenomena associated with the unsteady motion of the profile. However, no complete set of experimental data was found to cover a range of reduced frequencies at the same Reynolds and Mach numbers and, thus, only qualitative comparisons between the present calculations and Wilby's findings are possible. Our investigation is performed for a ramping NACA-0012. In all computations, the same values of the Mach and Reynolds numbers are used ($M = 0.302$, $Re_c = 4.5 \times 10^6$), while the pitch rate, k_f, varies from 2 to 0.1. Various models were initially tested, and it was found that the best compromise between accuracy and computational cost is obtained by the two-equation NLEVM. However, for angles of incidence up to about 16°, the one-equation Spalart–Allmaras model was found to give similar results; the linear EVMs were too dissipative, thus suppressing separation, especially at low pitch rates.

Figure 7 presents the time history of the lift coefficient as well as the instantaneous surface pressure distribution at the stall angle, for three different pitch rates $k_f = 2, 0.5$ and 0.1. Results are presented using the NLEVM of Craft *et al.* [26] and the Spalart–Allmaras [40] models. The main finding is that for pitch rates less than 0.5 the DSV is not present during the pitch. Instead, a trailing edge vortex was present. This is shown in Figure 7 in the instantaneous C_p curve at stall conditions. Moreover, at even lower pitch rates (Figure 7(c)) periodic shedding of vortices from the trailing edge was also encountered, leading subsequently to oscillating aerodynamic loads.

Several calculations were also performed to investigate the effects of the number of time steps on the predicted aerodynamic loads and Figure 6 shows the number of time steps as function of the pitch rate. To resolve the periodic shedding of vortices at lower pitch rates a much finer time resolution is required.

For all cases the stall angle is determined based on the change of sign of the derivative of the lift and moment curves and the results using the NLEVM and Spalart–Allmaras models are shown in Figure 6(c). The computations, especially those with the NLEVM, reveal a change of the curve slope at lower values of the pitch rate, and this is in agreement with Wilby's

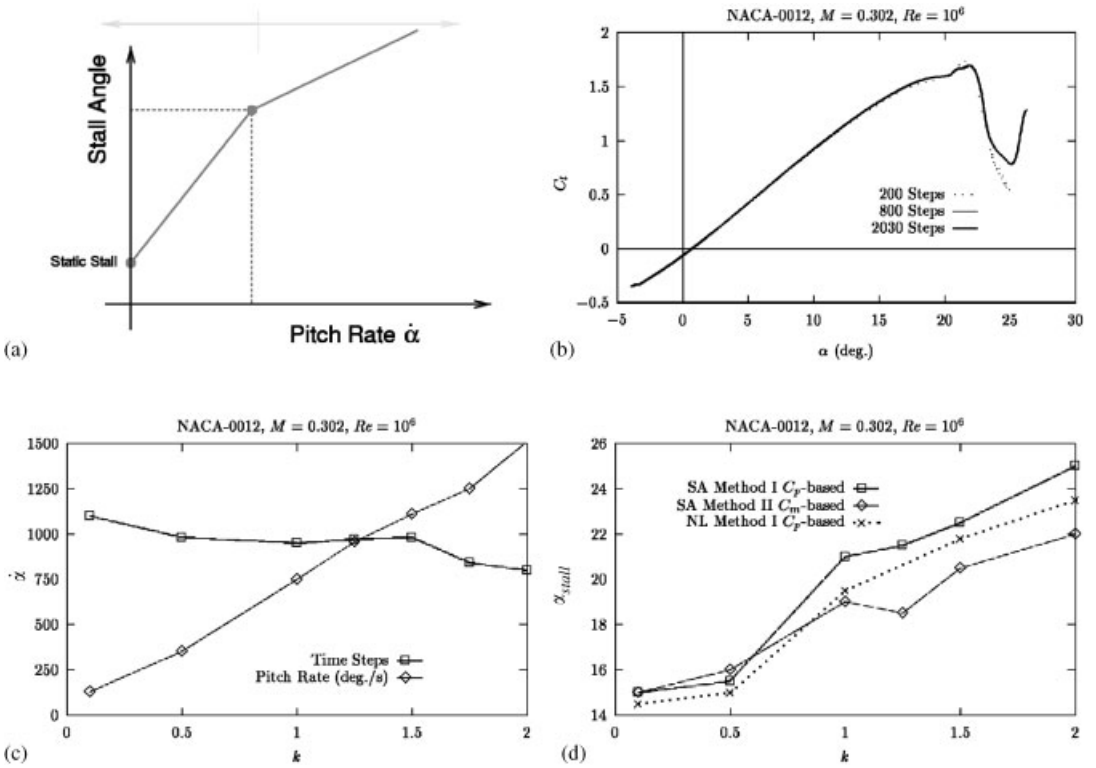

Figure 6. (a) Schematic of the variation of the stall angle with the pitch rate according to Wilby (1996); (b) effects of time-step on the predicted unsteady airloads of a ramping NACA-0012 aerofoil ($M = 0.302$, $Re = 10^6$, $\alpha_0 = -4^\circ$, $\alpha_1 = 30^\circ$, $k_f = 1.125$); (c) time steps required for convergence for different pitch rates, for the ramping NACA-0012 aerofoil; (d) numerical predictions of the variation of the stall angle with the pitch rate for a ramping NACA-0012 aerofoil.

findings [49]. Plate 1 shows the separated flow region on the suction side of the ramping profile for three values of the pitch rate. In these plots, the DSV, the trailing edge separation and the trailing edge vortices are shown. Further, the time histories of the pressure-coefficient distributions (Plate 1), suggest that there are differences in the DSV onset between lower and higher pitch rates. In the former case a vortex is formed at the trailing edge of the aerofoil as soon as the aerofoil reaches a certain incidence angle. The shedding of this vortex in the wake marks the stall of the aerofoil and this is very similar to the static stall. On the other hand, at higher pitch rates the DSV formed near the leading edge of the profile propagates downstream over the suction side of the aerofoil and is finally shed in the wake.

3.3. Further comments on the models performance

The CPU time for a single time step, as well as the number of time steps needed for every period of oscillation, depend strongly on the flow case and turbulence model employed. The one-equation model provides faster results compared to two-equation linear and non-linear

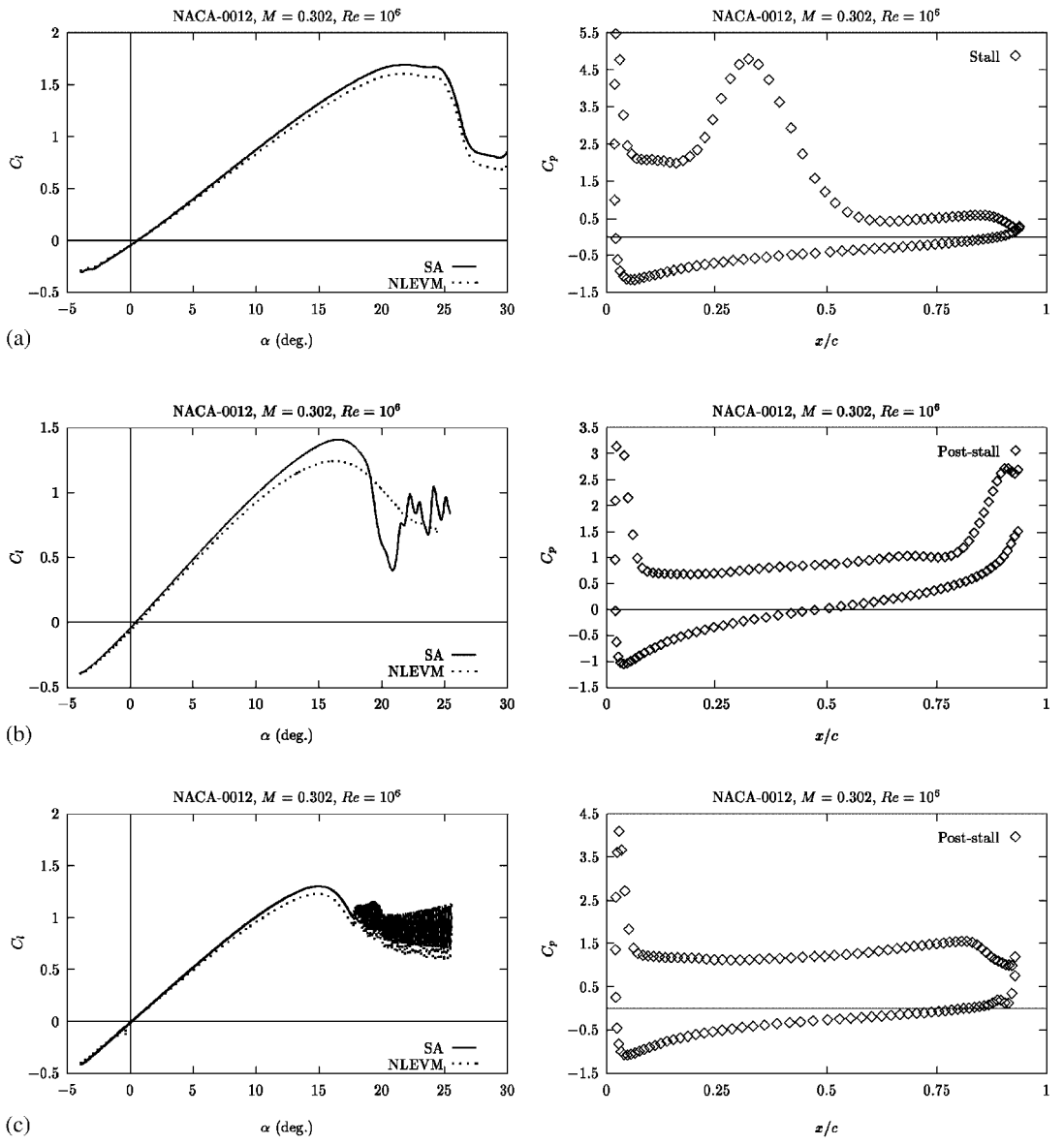

Figure 7. Time history of the lft coefficient (left) and instantaneous surface pressure distribution at stall angle (right) for a ramping NACA-0012 aerofoil with (a) $k_f = 2.0$, (b) $k_f = 0.5$ and (c) $k_f = 0.1$; $M = 0.302$, $Re = 10^6$, $\alpha_0 = -4^\circ$, $\alpha_1 = 30^\circ$; NL = non-linear model and SA = Spalart–Allmaras model.

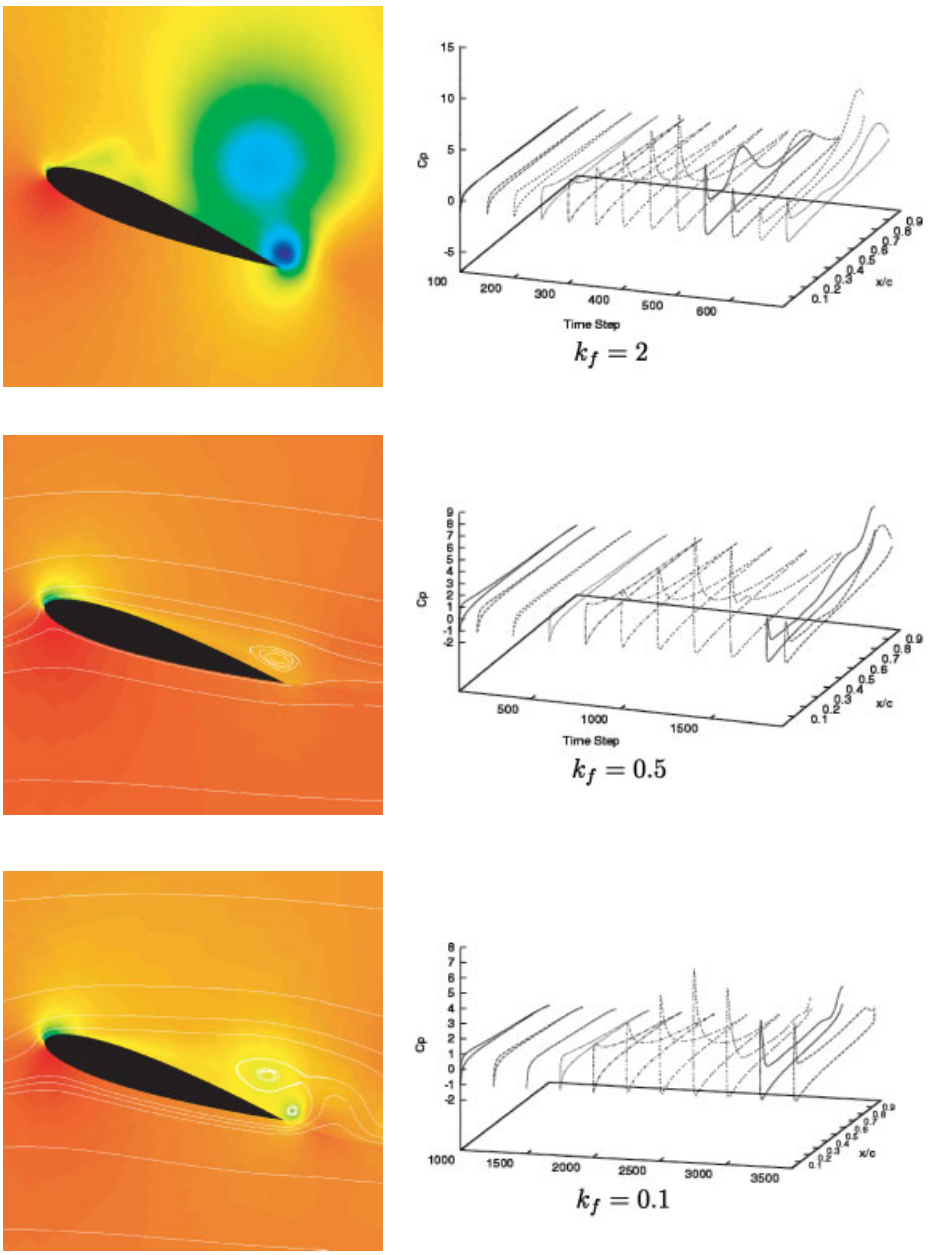

Plate 1. Density field near the stall incidence (left) and time history of the surface pressure distribution (right) around a ramping NACA-0012 aerofoil at various pitch rates ($M_\infty = 0.302,\ Re = 10^6,\ \alpha_0 = -4^\circ,\ \alpha_1 = 30^\circ$).

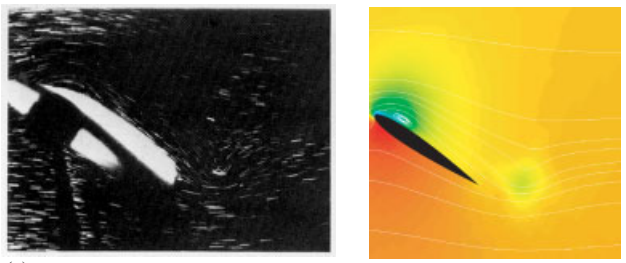

(a)

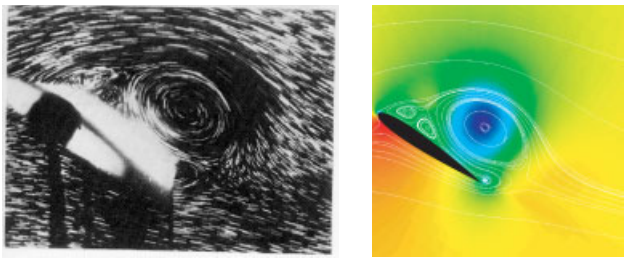

(b)

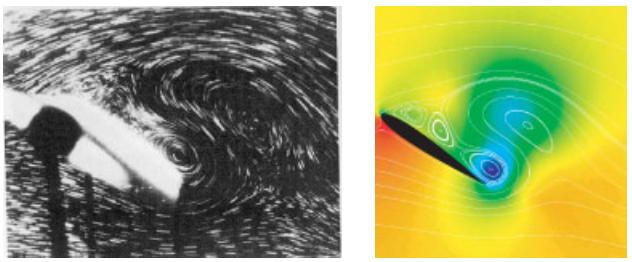

(c)

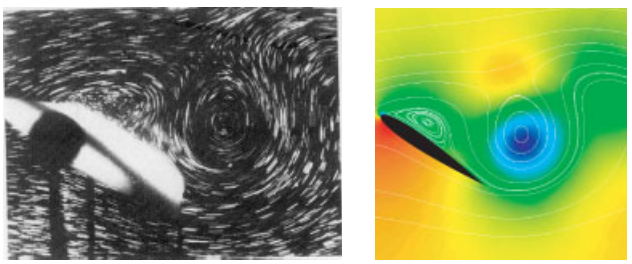

(d)

Plate 2. Startup of flow over a NACA-0012 aerofoil at high incidence angle ($Re = 1000,\ \alpha = 23^\circ$).

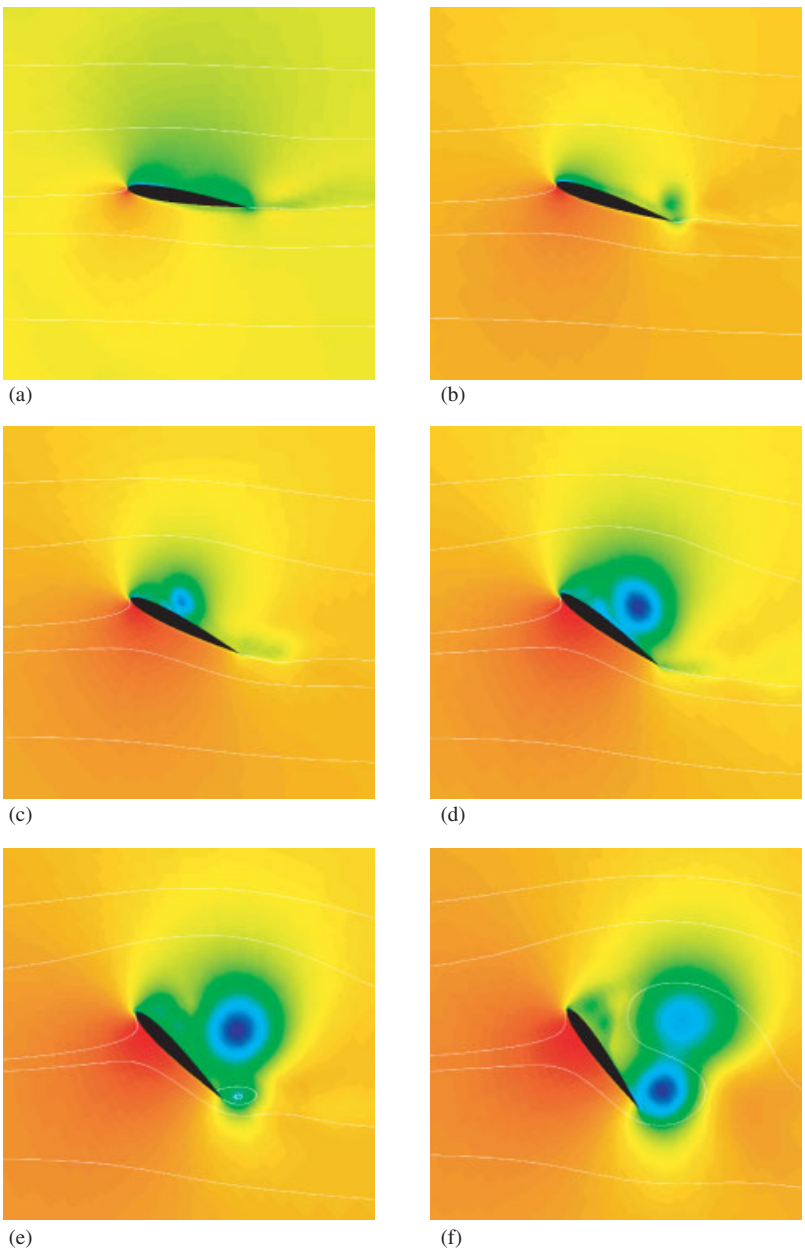

Plate 3. Density field around a ramping NACA-0012 aerofoil ($Re = 10^5$, $M = 0.25$, $k_f = 1$, $\alpha_{max} = 60^\circ$).

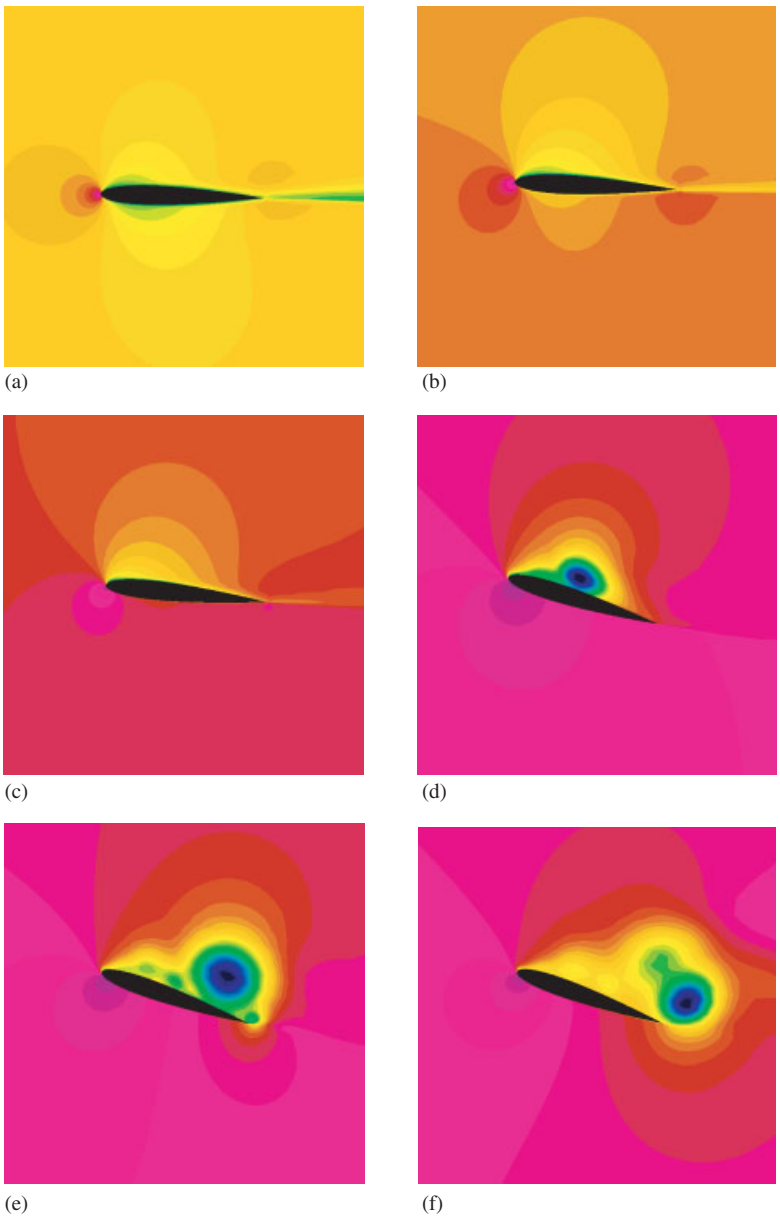

Plate 4. Density field around a harmonically oscillating NACA-0012 aerofoil ($Re = 10^6,\ M = 0.2,\ k_f = 0.2,\ \alpha_0 = 15^\circ,\ \alpha_1 = 10^\circ$).

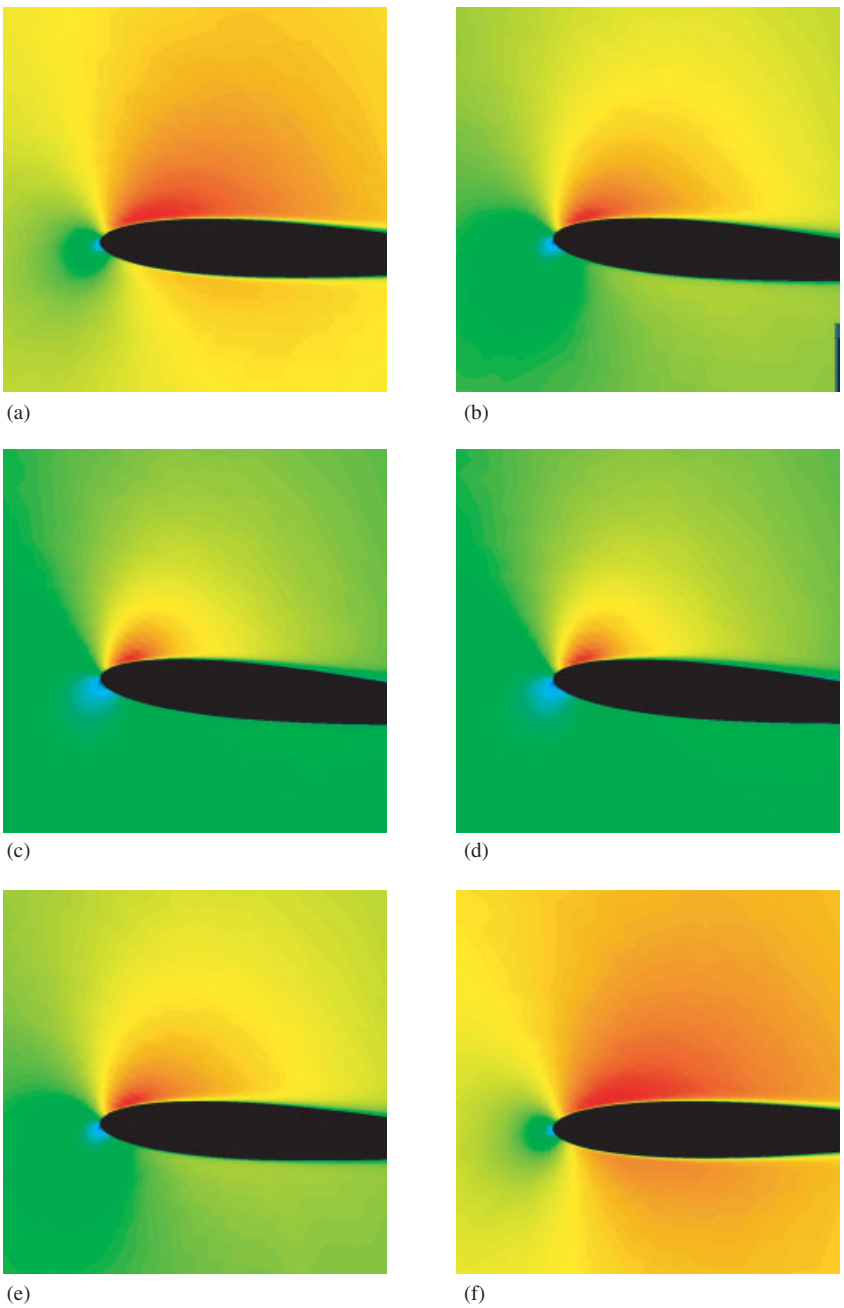

Plate 5. Mach number field around an oscillating NACA-0012 aerofoil; AGARD CT1 Case ($M = 0.6,\ Re_c = 4.8 \times 10^6,\ k_f = 0.16,\ \alpha_0 = 2.8^\circ,\ \alpha_1 = 2.4^\circ$).

models. For all unsteady cases examined in this work, three oscillation cycles were required to obtain the periodic loads. The number of time steps per oscillation cycle varied from 48 for the CT1 case to 145 for the deep-stall oscillation of the NACA-0012. The CPU time per step doubles when a two-equation model is employed instead of an algebraic one [22]. The NLEVM has been found to be more difficult to converge and requires a further reduction of the CFL number. For the most difficult case considered here (oscillating NACA-0012 at deep-stall conditions) about three to four days of CPU time on a single processor of a Silicon Graphics Origin 2000 machine, are required to obtain converged unsteady solutions using the NLEVM. The considerably increased CPU requirements for the NLEVM are due to the fact that the model increases the stiffness of the numerical solution and results, in general, in slower convergence rates.

4. FLOW DEVELOPMENT UNDER DYNAMIC-STALL CONDITIONS

In this section, we present results from the computational investigation of dynamic stall flows at various flow conditions.

There are several phenomena associated with the pitching motion of an aerofoil, the most important being the generation of intense vorticity over the suction surface near the leading edge. As the pitching motion goes on, the DSV is formed, detaches from the aerofoil and convects along the suction surface. The above are associated with large variations of the lift, drag and pitching moment coefficients. The DS evolves either with the generation of weaker vortices, if the aerofoil remains above its static angle of incidence (ramping case), or terminates if the aerofoil returns to an angle sufficiently small to allow re-attachment of the flow (oscillating case).

The flow visualization experiments of Daube *et al.* [52] regarding the startup of the flow around a NACA-0012 aerofoil have shown similarities between the development of the DS at laminar and turbulent flow conditions. Therefore, we initially performed calculations at laminar flow conditions and comparisons between the flow visualization of Daube *et al.* [52] and our computations are shown in Plate 2. The separation bubble formed at the leading edge of the aerofoil evolves to a big vortex over the suction side of the aerofoil (Plate 2(a)). As the vortex moves towards the trailing edge, two other vortices (Plate 2(b)) are formed in the neighbourhood of the leading edge. Additionally, at the trailing edge another vortex is formed as the result of the flow emerging from the pressure side of the profile (Plate 2(b)). The initially formed vortex is shed at the wake (Plate 2(c)) while the trailing edge vortex grows (Plate 2(d)) and subsequently dominates the region over the aerofoil. Then, a new leading edge vortex starts growing again to repeat eventually the unsteady cycle. The flow phenomena as described above are very similar to the ones described by McCroskey and Philippe [53] for the flow around a ramping aerofoil.

To examine the similarity of dynamic stall flows at laminar and turbulent flow conditions, we performed simulations around pitching and oscillating aerofoils at high Reynolds numbers. The density field around a ramping NACA-0012 aerofoil at various angles of incidence is shown in Plate 3. The dynamic-stall vortex emerging from the leading edge grows in size as the incidence increases. At higher incidence angles there are two other vortice, one formed at the leading edge upstream of the DSV, and another one that emerges from the trailing edge. Near the maximum incidence, both the DSV and the trailing edge vortices detach from the aerofoil's surface.

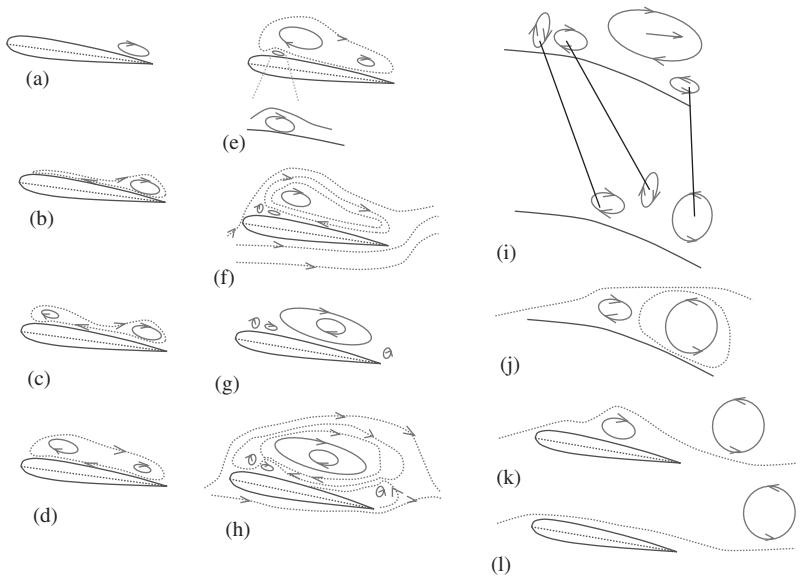

Figure 8. Flow topology around a harmonically oscillating aerofoil at (a) subsonic and (b) transonic turbulent flow conditions.

Further, the numerical flow visualizations for the harmonically oscillating NACA-0012 aerofoil at high-Reynolds number and deep stall conditions, discussed in the preceding section, are shown in Plate 4. The onset of the DSV is not different from the ramping case. At high incidence angles the vortical structure formed over the aerofoil is very similar to the one presented in the startup of the laminar flow and in the turbulent flow around the ramping NACA-0012. The only difference is that for the oscillating aerofoil the DSV is shed at the wake as the aerofoil begins the downstroke motion, and the flow starts to reattach at the leading edge. A comparison of the vortical structures for the startup of the flow as well as for the ramping and harmonically oscillating cases can be made by looking at Plates 2(b), 4(f) and 3(e), respectively.

The flow development for the above cases is different from the hysteresis flow presented in the preceding section for the AGARD CT1 case, where a weak shock is formed in the leading edge region (Plate 5). A consolidated qualitative representation of the flow phenomena appeared at subsonic and transonic flow conditions is given below. Figures 8 and 9 present the flow topology for the case of a harmonically oscillating aerofoil at subsonic turbulent flow conditions and harmonically oscillating aerofoil at transonic turbulent flow conditions, respectively. Both figures have been created by analysing results from various computations performed in this study and are abstractions of Figures 10 and 11 which present instantaneous streamtraces for a ramping NACA-0012 at low and high Mach numbers, respectively.

Both in subsonic and in transonic cases, generation of vorticity on the suction side of the aerofoil at the early stages of the upstroke motion occurs. Figures 8(a) and 9(b) show that separation starts at the trailing edge as a clockwise rotating vortex and, subsequently, leading

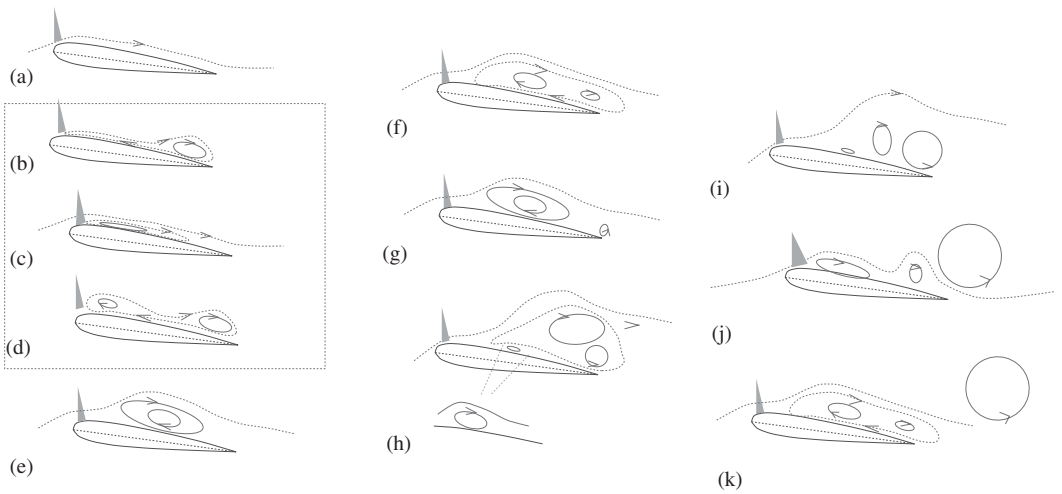

Figure 9. Flow topology around a harmonically oscillating aerofoil at transonic turbulent flow conditions.

edge separation occurs (Figures 8(c) and 9(c)). For rapidly pitching aerofoils, separation may start directly from the leading edge (Figure 9(c)). For high Mach numbers this situation is assisted by the shock formed close to the leading edge of the profile. As the upstroke motion continues the DSV is formed; the DSV is rotating clockwise and moves towards the trailing edge of the aerofoil (Figures 8(d) and 9(e)), while a smaller vortex simultaneously forms between the DSV and the aerofoil's wall (Figure 8(e)). Subsequently, this vortex breaks up into a pair of vortices. Further, a counter-clockwise rotating vortex forms at the trailing edge of the profile (Figures 8(g) and 9(h)) due to the roll-up of a fast moving stream of fluid emerging from the suction side of the profile. At maximum incidence angle the DSV is shed in the wake. During the downstroke motion of the aerofoil all vortices are shed in the wake and the flow gradually reattaches starting from the leading edge region (Figures 8(j)–8(l)). For higher Mach numbers the shock formed close to the leading edge of the profile may delay reattachement (Figure 9(j)). For the case of a ramping aerofoil there is no downstroke motion. At the maximum angle, the aerofoil remains steady and stalls.

The effects of the various flow structures on the aerodynamic loads are discussed below. Figure 12 presents the time history of the aerodynamic loads as predicted using the NLEVM. Figure 12(a) suggests that for the CT1 case (moderate Mach number, small mean angle and oscillation amplitude) there is a smooth variation of the C_p coefficient during the unsteady oscillation, thus, resulting in a simple hysteresis loop. Figure 12(b) presents the wall-pressure history for the NACA-0012 aerofoil harmonically oscillating at deep-stall subsonic conditions. It is evident that there is an abrupt change of the C_p coefficient as the maximum incidence is approached. The presence of the DSV is indicated by a second peak on the C_p curve (Figure 12(b)). The above flow behaviour is totally different from the static stall of an aerofoil where separation initially occurs at the trailing edge region and the stall angle is smaller. Figure 12(c) shows the history of the C_p coefficient for a harmonically oscillating NACA-0012 at low frequency. The conditions are close to those of the deep-stall oscillating NACA-0012 aerofoil, but the reduced frequency of oscillation is much smaller ($k_f = 0.05$). As shown,

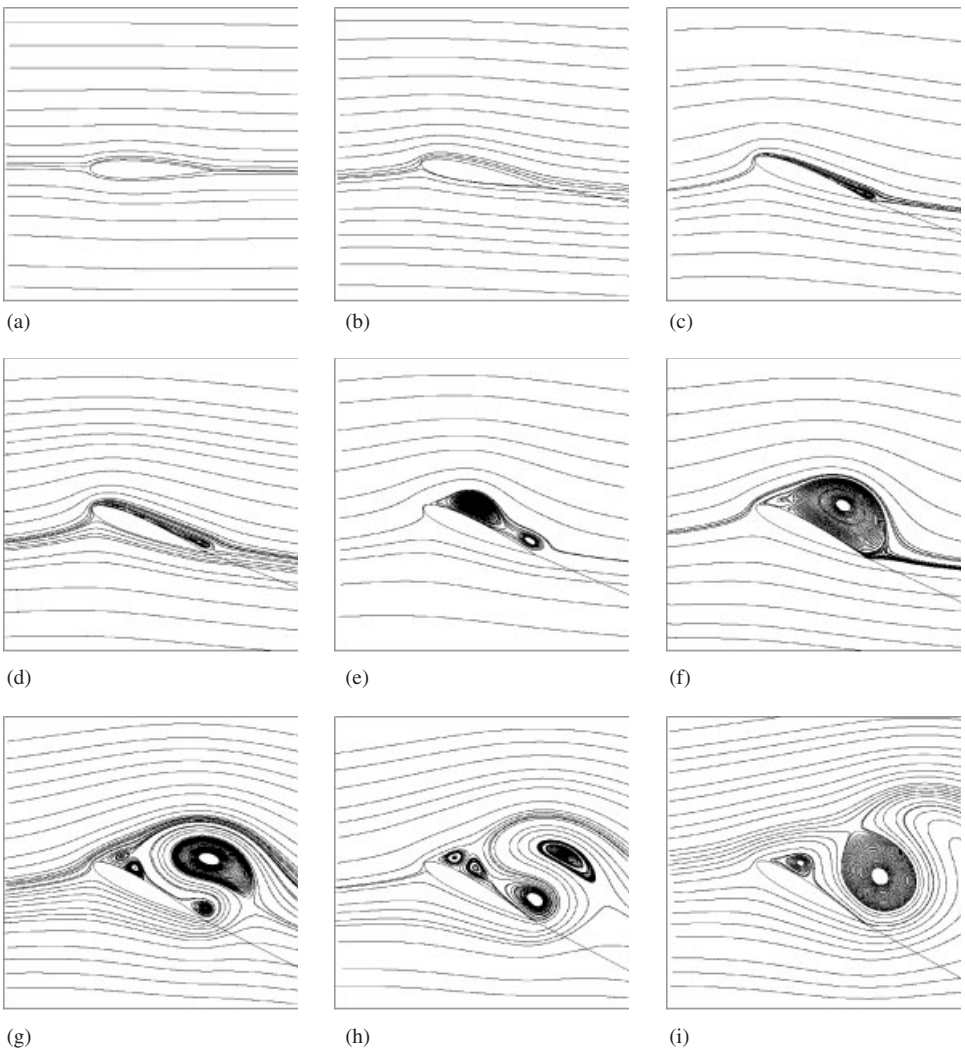

Figure 10. Evolution of the dynamic stall over a ramping NACA-0012 aerofoil at subsonic flow conditions ($Re = 4.5 \times 10^6$, $M = 0.302$, $\alpha_0 = -4^\circ$, $\alpha_1 = 30^\circ$, $k_f = 1.5$).

the DSV is not present and vortex shedding occurs directly at the trailing edge region as the stall-angle is approached. This is essentially a quasi-steady calculation—pitching at very low rate—and the stall angle is the static one. For a higher Mach number—case of ramping NACA-0012—separation of the boundary layer is associated both with the moving boundary and with the shock/boundary-layer interaction. Figure 12(d) shows the time history of the C_p for the case of the ramping NACA-0012. The presence of a shock is evident in the middle of the plot, at dimensionless time-step about 50 while vortex-shedding has started earlier. The path of the vortex around the aerofoil is not as clear as for the subsonic case, because for the ramping case flow separation starts downstream of the shock.

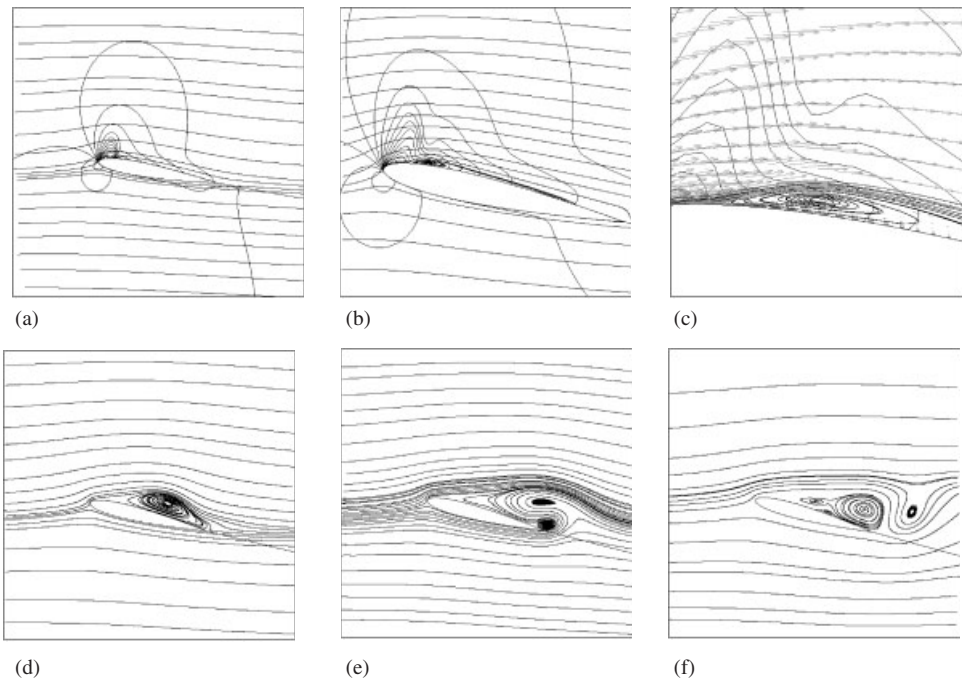

Figure 11. Evolution of the dynamic stall over a ramping NACA-0012 aerofoil at transonic flow conditions ($Re = 4.5 \times 10^6$, $M = 0.775$, $\alpha_0 = -4°$, $\alpha_1 = 30°$, $k_f = 1.5$).

5. CONCLUDING REMARKS

A computational study of dynamic-stall flows at subsonic and transonic Mach numbers was presented. The investigation was based on an implicit-unfactored solver and a Godunov-type scheme which solve the Navier–Stokes and turbulence-transport equations in a strongly coupled fashion. Several turbulence closures were implemented in conjunction with the above method and assessed for a broad range of dynamic stall flows around pitching and oscillating aerofoils. The NLEVM model provided better results than the linear EVMs and was able to capture, at least qualitatively, the most important flow phenomena occuring around pitching and oscillating aerofoils, such as the DSV, leading and trailing edge separation, hysteresis of the airloads, as well as associated unsteady shock/boundary-layer interaction in the transonic regime. It was also found that the one-equation Spalart–Allmaras model performed well at angles of incidence below 16°.

Depending on the frequency of the unsteady motion of the lifting surface, dynamic or static stall can be obtained. For rapidly moving lifting surfaces the DSV originates from the leading edge. The computations revealed strong similarities regarding the onset of dynamic stall at laminar and turbulent flow conditions, as well as between pitching and oscillating aerofoils. In the case of oscillating aerofoils, the DSV is shed in the wake as the aerofoil executes downstroke motion and the flow starts to reattach at the leading edge. For a certain range of transonic Mach numbers, it was found that there is a change of the stall angle. This is

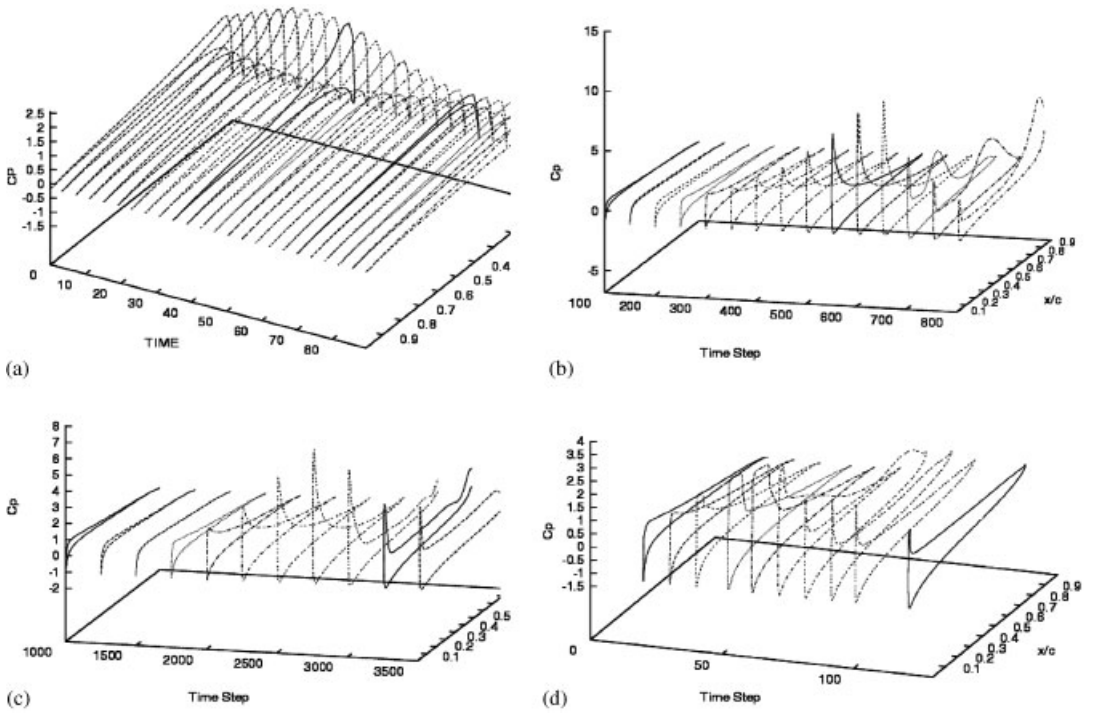

Figure 12. Surface pressure histories: (a) AGARD CT1 case, (b) oscillating NACA-0012 at deep-stall conditions, (c) oscillating NACA-0012 at low frequency, and (d) ramping NACA-0012.

probably due to the shock/boundary-layer interaction occuring near the leading edge of the aerofoil. For small mean angle and oscillation amplitudes there is a smooth variation of the pressure-coefficient distribution on the aerofoil's surface and the variation of the aerodynamic loads are represented by a simple hysteresis loop. On the other hand, at deep-stall conditions more complex variations of the aerodynamic loads occur due to the intense activation of several vortices originating from the leading and trailing edges of the aerofoil.

The computations regarding the effects of the reduced frequency on the stall-angle, were found to be in good qualitative agreement, especially in the case of the NLEVM, with previous experimental studies [49]. The computations revealed differences between low and high pitch rates. In the former case, a vortex is formed at the trailing edge of the aerofoil as soon as the aerofoil reaches a certain incidence angle. The shedding of this vortex in the wake marks the stall of the aerofoil and this is very similar to the static stall. On the other hand, at high pitch rates the flow is dominated by the DSV originating from the leading edge, which propagates downstream over the suction side of the aerofoil and is finally shed in the wake.

ACKNOWLEDGEMENTS

Various parts of this work were supported by the following projects: (i) EPSRC/MoD (GR/L18457) in collaboration with GKN Westland Helicopters and (ii) Brite/EuRam project UNSI.

The UNSI project (unsteady viscous flow in the context of fluid–structure interaction) is a collaboration between Alenia, BAe, CASA, Dasa-M (Coordinator), Dassault, DERA, DLR, FFA, IMFT, IRPHE, NUMECA, ONERA, Saab, TUB and QMW. The project is funded by the European Union and administrated by the CEC, DG XII, Brite/EuRam, IMT (Project Ref: BRPR-CT97-0583).

REFERENCES

1. Telionis DP. Unsteady boundary layers, separated and attached. *AGARD Conference Proceedings 227*, Paper 16, 1977.
2. McCroskey WJ. The phenomenon of dynamic stall. *NASA Technical Memorandum* 81264, 1981.
3. McCroskey WJ, McAlister KW, Carr LW, Pucci SL. An experimental study of dynamic stall on advanced airfoil sections. Volume 1: Summary of the experiment. *Technical Memorandum* 84245, Vol. 1, NASA, 1982.
4. Maresca C, Favier D, Rebont J. Experiments on an aerofoil at high angle of incidence in longitudinal oscillations. *Journal of Fluid Mechanics* 1979; **92**:671–690.
5. Favier D, Maresca C, Renon P. Étude du comportement de la couche limite sur un modéle oscillant par vélocimétrie Laser embarquée. *28 Colloqe d'Aerodynamique Appliquée de L'Association Aéronautique et Astronautique de France*, Saint-Louis, 1991.
6. Piziali RA. An experimental investigation of 2D and 3D oscillating wing aerodynamics for a range of angle of attack including stall. *NASA Technical Memorandum* 4632, 1994.
7. Doligalski TL, Smith CR, Walker JDA. Vortex interactions with walls. *Annual Review of Fluid Mechanics* 1994; **26**:573–616.
8. Smith FT. Concerning dynamic stall. *Aeronautical Quarterly* 1982; **33**:331–352.
9. Peridier V, Smith F, Walker J. Vortex induced boundary layer separation. Part 1. The limit problem $Re \rightarrow \infty$. *Journal of Fluid Mechanics* 1991a; **232**:99–131.
10. Mehta UB, Lavan Z. Starting vortex, separation bubbles and stall: A numerical study of laminar unsteady flow around an airfoil. *Journal of Fluid Mechanics* 1975; **67**:227–256.
11. Visbal MR. On the formation and control of the dynamic stall vortex on a pitching airfoil. *AIAA Paper* 91-0006, 1991.
12. Choudhuri PG, knight DD. Effects of compressibility, pitch rate and Reynolds number on unsteady incipient boundary layer separation over a pitching airfoil. *Journal of Fluid Mechanics* 1996; **308**:195–217.
13. Tuncer IH. Unsteady aerodynamics of oscillating and rapidly pitched airfoils. *Ph.D. Thesis*, Georgia Institute of Technology, 1988.
14. Carr LW. Progress in analysis and prediction of dynamic stall. *Journal of Aircraft* 1998; **25**(1):6–17.
15. Visbal MR. Effect of compressibility on dynamic stall. *AIAA Paper* 88-0132, 1998.
16. Ekaterinaris JA. Numerical investigation of dynamic stall of an oscillating wing. *AIAA Journal* 1995; **33**(10):1803–1808.
17. Guilmineau E, Piquet J, Quentey P. Two-dimensional turbulent viscous flow simulation past airfoils at fixed incidence. *Computers and Fluids* 1997; **26**(2):135–162.
18. Kermarec M, Decaix AF, Renon P, Favier D, Maresca C. Numerical modelling of unsteady flows around airfoils by a coupled potential-boundary-layer method. *European Journal of Mechanics B/Fluids* 1993; **12**(5):657–681.
19. Badcock KJ, Cantariti F, Hawkins I, Woodgate M, Dubuc L, Richards BE. Simulation of unsteady turbulent flows around moving aerofoils using the pseudo-time method. *International Journal for Numerical Methods in Fluids* 2000; **32**(5):585–604.
20. Barakos G, Drikakis D. An implicit unfactored method for unsteady turbulent compressible flows with moving boundaries. *Computers and Fluids* 1999; **28**(8):899–921.
21. Barakos G, Drikakis D. Separated turbulent flows over maneuvering lifting surfaces. *Philosophical Transactions of the Royal Society of London A*: *Mathematical Physical and Engineering Sciences* 2000c; **358**(1777) (Issue 15th):3279–3292.
22. Baldwin BS, Lomax H. Thin layer approximation and algebraic model for separated turbulent flows. *AIAA Paper* 78-257, 1978.
23. Davidson L. Reynolds stress transport modelling of shock-induced separated flow. *Computers and Fluids* 1995; **24**(3):253–268.
24. Batten P, Craft TJ, Leschziner MA, Loyau H. Reynolds-stress-transport modeling for compressible aerodynamics applications. *AIAA Journal* 1999; **37**(7):785–797.
25. Speziale CG. On nonlinear K–l and K–ε models of turbulence. *Journal of Fluid Mechanics* 1987; **178**: 459–475.
26. Craft TJ, Launder BE, Suga K. Development and application of a cubic eddy-viscosity model of turbulence. *International Journal of Heat and Fluid Flow* 1996; **17**(2):108–115.
27. Gatski TR. Prediction of airfoil characteristics with high order turbulence models. *NASA Technical Memorandum* 110246, NASA, 1996.

28. Abid R, Rumsey C, Gatski T. Prediction of nonequilibrium turbulent flows with explicit algebraic stress models. *AIAA Journal* 1995; **33**(11):2026–2031.
29. Abid R, Morrison JH, Gatski TB, Speziale CG. Prediction of aerodynamic flows with a new explicit algebraic stress model. *AIAA Journal* 1996; **34**(12):2632–2635.
30. Pope SB. A more general effective–viscosity hypothesis. *Journal of Fluid Mechanics* 1975; **72**(Part 2):331–340.
31. Speziale CG, Ngo T. Numerical solution of turbulent flow past a backward-facing step using a non-linear k–ε model. *International Journal of Engineering Science* 1988; **26**:1099–1112.
32. Shih T-H, Zhu J, Lumley JL. A realizable Reynolds stress algebraic equation model. *NASA Technical Memorandum* 105993, 1993.
33. Jiang YT, Damodaran M, Lee KH. High-resolution finite volume computation of turbulent transonic flow past airfoil. *AIAA Journal* 1997; **35**(7):1134–1142.
34. Barakos G, Drikakis D. Investigation of non-linear eddy-viscosity turbulence models in shock-boundary layer interaction. *AIAA Journal* 2000; **38**(3):461–469.
35. Barakos G, Drikakis D. Numerical simulation of buffeting flows using various turbulence closures. *International Journal of Heat and Fluid Flow* 2000; **21**(5–6):620–626.
36. Craft TJ, Launder BE, Suga K. A non-linear eddy-viscosity model including sensitivity to stress anisotropy. *Proceedings of the 10th Symposium on Turbulent and Shear Flows* 1995; 23-19–23-24.
37. Brenneis A, Eberle A. Application of an implicit relaxation method solving the Euler equations for time-accurate unsteady problems. *Journal of Fluids Engineering* 1990; **112**(4):510–520.
38. Barakos G, Drikakis D. Implicit-coupled implementation of two-equation turbulence models in compressible Navier–Stokes methods. *International Journal for Numerical Methods in Fluids* 1998; **28**(1):73–94.
39. Fan S, Lakshminarayana B, Barnett M. Low-Reynolds-number k–ε model for unsteady turbulent boundary-layer flows. *AIAA Journal* 1993; **31**(10):1777–1784.
40. Spalart PR, Allmaras SR. A one-equation turbulence model for aerodynamic flows. *AIAA Paper* 92-0439, 1992.
41. Launder BE, Sharma BI. Application of the energy-dissipation model of turbulence to the calculation of flow near a spinning disk. *Letters in Heat and Mass Transfer* 1974; **1**:131–138.
42. Suga K. Development and application of a non-linear eddy viscosity model sensitized to stress and strain invariants. *Ph.D. Thesis*, University of Manchester Institute of Science and Technology, 1995.
43. Launder BE, Shima N. Second-moment closure for the near-wall sublayer: development and application. *AIAA Journal* 1989; **27**(10):1319–1325.
44. Drikakis D, Durst F. Investigation of flux formulae in transonic shock wave/turbulent boundary layer interaction. *International Journal for Numerical Methods in Fluids* 1994a; **18**(4):385–413.
45. Drikakis D, Durst F. A numerical study of viscous supersonic flow past a flat plate at large angles of incidence. *Physics of Fluids* 1994b; **6**(4):1553–1573.
46. Eberle A. Characteristic flux averaging approach to the solution of Euler's equations. *Lecture No. 1987-04 in VKI Series in Computational Fluid Dynamics*, VKI, 1987.
47. Sorenson RL. A computer program to generate two-dimensional grids about airfoils and other shapes by the use of Poisson's equation. *NASA Technical Memorandum* 81198, 1980.
48. AGARD, Various authors. Compendium of unsteady aerodynamic measurements. *AGARD Advisory Report* AR-702, 1982.
49. Wilby PG. The development of rotor aerofoil testing in the UK—The creation of a capability to exploit a design opportunity. *Proceedings of the 1996 European Rotorcraft Forum* 1996; 18-1–18-11.
50. Mabey DG, Welsh BL, Pyne CR. A summary of measurements of steady and oscillatory pressures on a rectangular wing. *Aeronautical Journal* 1998; **92**:10–28.
51. Chandrasekhara MS, Wilder MC, Carr LW. Competing mechanisms of compressible dynamic stall. *AIAA Journal* 1998; **36**(3):387–393.
52. Daube O, TaPhuoc L, Monnet P, Coutanceau M. Ecoulement instationaire décollé d'un fluide incompressible autour d'un profile d'aile: une comparaison théorie—expérience. *AGARD Conference Proceedings CP-386*, Paper No. 3, 1985 (in French).
53. McCroskey WJ, Philippe JJ. Unsteady viscous flow on oscillating airfoils. *AIAA Journal* 1975; **13**(1):71–79.

